

# Effect of Cerium on the Austenitic Nucleation and Growth of High-Mo Austenitic Stainless Steel



QI WANG, LIJUN WANG, WEI ZHANG, JIANMIN LI, and KUOCHIH CHOU

The influence of small amounts of cerium on the solidification phenomena of S31254 high-Mo austenitic stainless steel was investigated by *in situ* observations and theoretical calculations. *In situ* observations indicate that cerium addition in molten steel can accelerate austenitic nucleation but inhibit primary austenite grain growth. The initial nucleation temperature occur 32.3 °C in advance and the nucleation site density increases to 176/mm after 2 seconds in S31254-Ce compared to S31254. The modified Ce-containing inclusions in S31254-Ce improve the ability for austenite heterogeneous nucleation, which would significantly reduce the energy barrier of nucleation. The nucleation mechanism obtained from Johnson–Mehl–Avrami–Kologoromov (JMAK) theory is changed from site saturation nucleation to site saturation plus Avrami nucleation after cerium addition. Furthermore, cerium addition also prolongs the whole solidification temperature range from 28 °C to 43.9 °C and limits the growth velocity of a single austenite grain from approximately 20 to 2 μm/s. The ratio of the solid phase decreases from 60 to 8.2 pct, but the grain density increases from 68.8 to 280/mm<sup>2</sup>, with the solidification time extended to 8 seconds after cerium addition. Thus, the main solidification behavior in the early solidification stage of S31254-Ce is nucleation instead of primary grain growth. The low growth velocity for austenite grains and significant high nucleation site density exhibit a low rate constant *k* during the solidification process. Moreover, cerium addition could significantly refine the solidified structure, and the grain density of the final solidified structure in S31254-Ce is 366.6/mm<sup>2</sup>.

<https://doi.org/10.1007/s11663-020-01798-9>

© The Minerals, Metals & Materials Society and ASM International 2020

## I. INTRODUCTION

HIGH-MO austenitic stainless steel (HMASS) has high concentrations of alloying elements (> 40 pct), especially Cr and Mo. This steel is believed to have great potential for application in extremely harsh service environments, such as seawater handling systems, chemical processing equipment, waste incineration systems and plate heat exchangers.<sup>[1,2]</sup> However, a higher Mo content is more likely to induce segregation due to the low partition coefficients at the liquid/austenite interface.<sup>[3]</sup> Center segregation is the main pattern of Mo macrosegregation through a numerical simulation

of the ingot pouring process.<sup>[4]</sup> The Mo-rich region in HMASS is susceptible to the formation of sigma phases, which results in difficulties in hot working processes.<sup>[5]</sup> Sigma in HMASS is a hard and brittle phase, and it may fracture during deformation, potentially initiating cracks or widening into interparticle voids during continued deformation.<sup>[6]</sup> The grains of HMASS are easy to grow during welding solidification, and this steel would be more sensitive to the precipitation of secondary phases ( $\sigma$ ,  $\chi$  and Laves phases).<sup>[7]</sup> Thus, the elimination of Cr and Mo segregation is critically important to improve the performance homogeneity of HMASS.

To obtain the optimum hot workability, homogenization heat treatment is necessary after casting. Zhu *et al.*<sup>[4]</sup> indicated that the residual microsegregation can be either minimized or eliminated by homogenization heat treatment; however, it should be noted that it is virtually impossible to eliminate Mo macrosegregation due to the distances over which Mo is required to transfer. A feasible method to reduce the diffusion distance is refining the solidification structure. The currently available grain refinement techniques used during steel casting can be categorized into three groups: electromagnetic stirring (EMS), fast cooling and

---

QI WANG and LIJUN WANG are with the The Collaborative Innovation Center of Steel Technology, University of Science and Technology Beijing, Beijing 100083, P.R. China. Contact e-mail: lijunwang@ustb.edu.cn KUOCHIH CHOU is with the The Collaborative Innovation Center of Steel Technology, University of Science and Technology Beijing and also with the The State Key Laboratory of Advanced Metallurgy, University of Science and Technology Beijing, Beijing, 100083, PR China. WEI ZHANG and JIANMIN LI are with the The Technical Center, Taiyuan Iron and Steel (Group) Co., Ltd, Taiyuan, 030003 Shanxi Province, P.R. China.

Manuscript submitted June 24, 2019.

Article published online February 21, 2020.

chemical grain refinement.<sup>[8]</sup> However, EMS and fast cooling is limited by the actual casting equipment. Therefore, chemical metallurgical methods including oxide metallurgy are commonly used for grain refinement. Inclusion-assisted microstructure control has been a key technology to improve the mechanical properties of steel. Inclusion may act as nucleation sites for heterogeneous nucleation to promote liquid to solid phase transformations during casting,<sup>[9–13]</sup> induce intragranular ferrite formation in the welding heat-affected zone,<sup>[14–18]</sup> and pin austenite grains, thereby preventing grain growth during the heat treatment process.<sup>[19,20]</sup>

Park *et al.*<sup>[9]</sup> and Guo *et al.*<sup>[21]</sup> noted that REM inclusions can refine macroscopic solidification structures in low-alloy steel. Cai *et al.*<sup>[22]</sup> indicate that cerium from the flux layers to weld metals can effectively refine the microstructure of the weld and promote the nucleation of acicular ferrites in BS700MC steel. Eijk *et al.*<sup>[23]</sup> analyzed the formation of Ce-Al-oxide inclusions in liquid S31254 stainless steel prior to solidification, which have good crystallographic compatibility with austenite. In summary, many studies performed by previous researchers mainly focused on the effects of various RE inclusions on crystal nucleation in low-alloy steel, whereas the application of cerium addition on the high alloy austenite stainless steel solidification process was rarely involved.

The common methods to investigate solidification behavior include liquid quenching, thermal-analysis technology and mold filling. However, these methods are indirect methods to confirm solidification and always have discrepancies in analyzing the solidification process. High-temperature laser scanning confocal microscopy (HT-LSCM) is an *in situ* analysis method, which has been implemented to observe the solidification process. HT-LSCM offers a great capability for real-time analysis, different cooling rates and continuous observations of phase transformations at high temperatures.<sup>[24]</sup> Therefore, it is of great interest to perform an *in situ* observation of the HMASS solidification process.

In the present study, the purpose is to investigate the influence of cerium addition on solidification phenomena, which can further show the function of cerium addition on austenite nucleation and growth in S31254 high-Mo austenitic stainless steel.

## II. MATERIALS AND EXPERIMENTAL METHODS

For the experiments with cerium addition, the S31254 high-Mo austenitic stainless steel samples (400 g) were contained in a MgO crucible ( $\Phi L50$ ) and placed in a vertical MoSi<sub>2</sub> resistance furnace ( $\Phi L90$ ). The schematic diagram of the experimental device used in this work is

shown in our former study.<sup>[25]</sup> The temperature of the liquid steel was maintained at 1500 °C under a high-purity Ar atmosphere (Ar 99.999 pct). To protect the cerium metal (99.9 pct purity, Aladdin) from oxidation, the metal was wrapped in a reduced iron powder and pressed into a metal cylinder, and then, the metal cylinder that was wrapped in pure iron chips was added to the molten steel. Good cerium homogeneity was achieved in the molten steel by stirring the molten steel for 15 seconds with a quartz tube. Table I shows the compositions of the steel samples, which were analyzed by ICP (Plasma1000, NCS).

*In situ* solidification observation was conducted on a HT-LSCM (VL2000DX-SVF17SP). The reaction chamber was vacuumed to 100 mPa and refilled with high-purity Ar (Ar 99.999 pct) three times. The temperature control system of the HT-LSCM was calibrated properly by a standard thermocouple. The samples, 7.5 mm in diameter and 3.5 mm thick, were placed in the aluminum crucible, which was inserted into the furnace. The sample was heated to 1450 °C at a rate of 200 °C/min and held isothermally for 5 min. The cooling rate was set to 50 °C/min to investigate the solidification behavior in all of the samples, and each experiment was repeated twice.

To observe the inclusions in the steel, the steel sample was ground to 2000 grit using SiC abrasive papers and then polished with diamond paste. The chemical compositions and morphologies of inclusions were analyzed through scanning electron microscopy and energy dispersive spectroscopy (SEM-EDS, Zeiss G500). Each sample was observed with 15 fields of view under magnification 1000 times.

## III. RESULTS AND DISCUSSION

### A. *In Situ* Observations

As mentioned previously, due to the  $C_{req}/N_{ieq} = 0.95$  in S31254 ( $C_{req} = Cr + Mo + 1.5Si$ ,  $N_{ieq} = Ni + 30C + 30N + 0.5Mn$ ), this steel solidification type belongs to the A mode, *i.e.*, only  $L \rightarrow \gamma$ . Figure 1 illustrates the solidification processes of S31254 obtained by HT-LSCM. The variations in the temperature and time duration are also displayed on the continuously recorded pictures. The white irregular particles and black areas in the pictures are solid phases, and the white areas are liquid phases. As shown in Figure 1(a), the initial nucleation site appears at 1382.9 °C. Two seconds later, the nucleation site density is increased to 13.32/mm<sup>2</sup>. As the temperature decreases, 60 pct solid phase is formed within 8 second in Figure 1(c). At the end, the solidus temperature is 1354.9 °C. The temperature range and entire time of

Table I. The Chemical Composition of the S31254 High-Mo Austenitic Stainless Steels

| Wt Pct    | Cr   | Ni   | Mo  | N    | Cu  | Si  | Mn  | C     | Al   | Ce    | Fe   |
|-----------|------|------|-----|------|-----|-----|-----|-------|------|-------|------|
| S31254    | 20.1 | 18.2 | 6.0 | 0.21 | 0.5 | 0.5 | 0.7 | 0.015 | 0.01 | 0     | bal. |
| S31254-Ce | 20.1 | 18.2 | 6.0 | 0.21 | 0.5 | 0.5 | 0.7 | 0.015 | 0.01 | 0.013 | bal. |

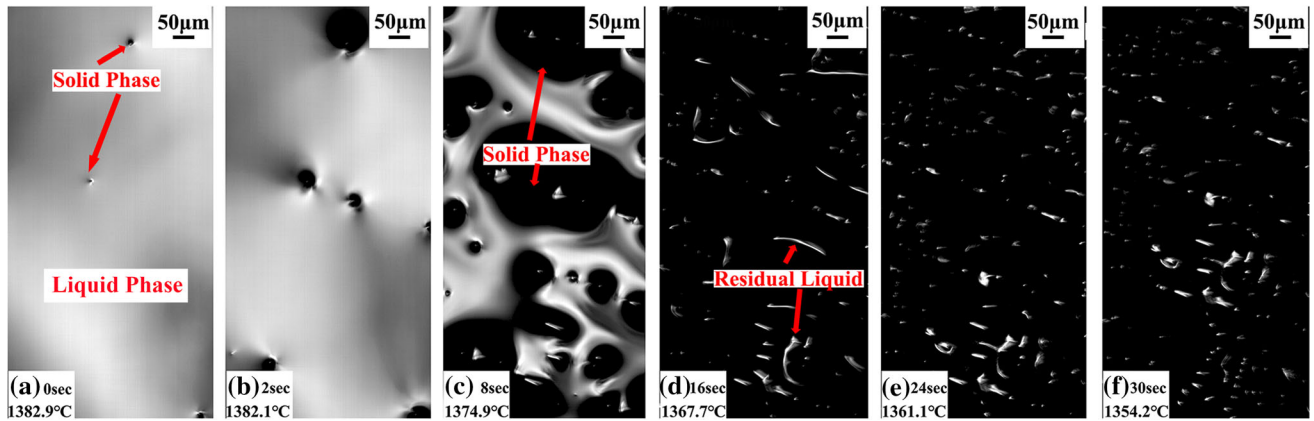


Fig. 1—Solidification process of S31254 observed *in situ* via HT-LSCM and cooled at 50 °C/min. The 6 features of interest areas follows: (a) and (b) primary austenite starts to nucleate; (c) continual growth of austenite grains; (d) the end stage of solidification with residual liquid; and (e) and (f) the sample is completely solidified.

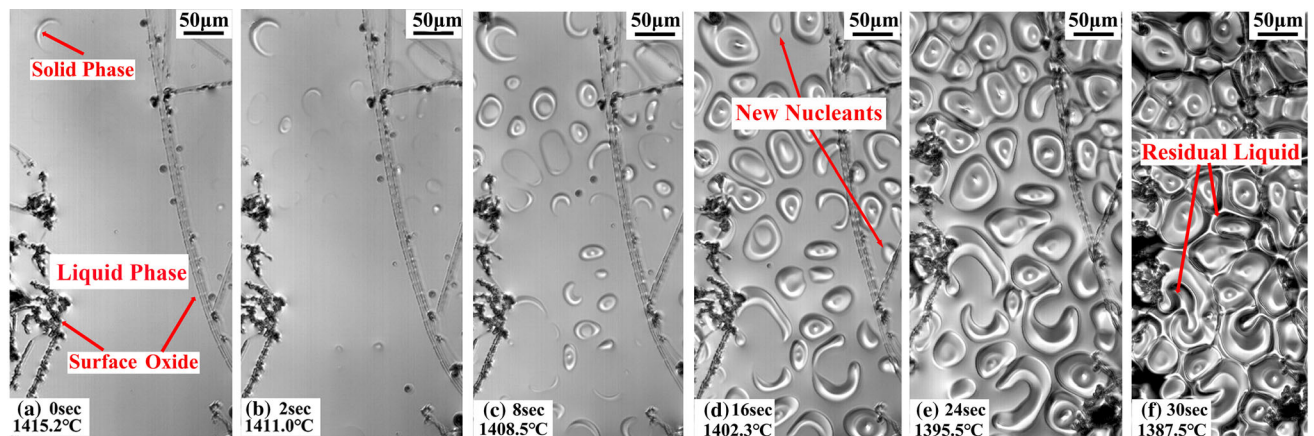


Fig. 2—Solidification process of S31254-Ce observed *in situ* via HT-LSCM and cooled at 50 °C/min: (a) primary austenite starts to nucleate, and some surface oxide can be observed; (b) to (d) nucleation and continual growth of austenite; (e) continual growth of austenite grains; and (f) residual liquid is solidified at the end stage of solidification, and several crescent-shaped austenite grains still exist in the final solidified microstructure.

solidification are 28 °C and 29.5 seconds, respectively. Figure 1 shows that the solidification of S31254 commenced below the surface of the opaque melt and was gradually shown on the melt surface.

Figure 2 gives the solidification process of S31254 with the addition of cerium. It shows quite a different solidification morphology. First, the initial nucleation site appeared at 1415.2 °C, which is 32.3 °C earlier than that of S31254. Two seconds later, the nucleation site density increased dramatically to 176/mm<sup>2</sup>, which is 162.68/mm<sup>2</sup> higher than that of S31254. It is apparent that the addition of cerium is highly beneficial for the nucleation process. The solidus temperature is changed to 1371.3 °C in S31254-Ce. The temperature range and entire time of solidification are 43.9 °C and 50.2 seconds, respectively. When the solidification time is extended to 8 seconds, only 8.2 pct solid phase formed, which is 51.8 pct lower than that of S31254. However, the grain density is enhanced from 68.8 to 280/mm<sup>2</sup>, which is shown in Figures 1(c) and 2(c). Thus, the main solidification behavior in the early solidification stage of

S31254-Ce is nucleation instead of primary grain growth. The grain density of the final solidified structure in S31254-Ce is obtained from Figure 2(f), and the measurement result is 366.6/mm<sup>2</sup>. Thus, 0.013 pct cerium addition could significant refine the solidified structure. The analysis results are shown in Table II. Furthermore, cerium is a surface active element, which would reduce the steel surface tension and further restrain solidification shrinkage. Crescent-shaped primary austenite and some surface oxides can be observed in Figure 2.

#### B. Quantification Analysis of the Nucleation and Growth Process by Using the JMAK theory

The solid volume in each case has been obtained *via* ImageJ software. The relationship between the solid volume fraction and time are plotted in Figure 3. Polycrystalline solidification is a type of first-order phase transformation proceeding *via* nucleation and growth. The kinetics of such transformations are often

**Table II. Analysis Results of Solidification Process**

|           | T <sub>n</sub> (°C) | T <sub>s</sub> (°C) | ΔT (°C) | Grain Density (2 s)   | Grain Density (8 s)  | Solid Ratio (8 s) | t <sub>total</sub> (s) |
|-----------|---------------------|---------------------|---------|-----------------------|----------------------|-------------------|------------------------|
| S31254    | 1382.9              | 1354.9              | 32.3    | 13.32/mm <sup>2</sup> | 68.8/mm <sup>2</sup> | 60 pct            | 29.5                   |
| S31254-Ce | 1415.2              | 1371.3              | 43.9    | 176/mm <sup>2</sup>   | 280/mm <sup>2</sup>  | 8.2 pct           | 50.2                   |

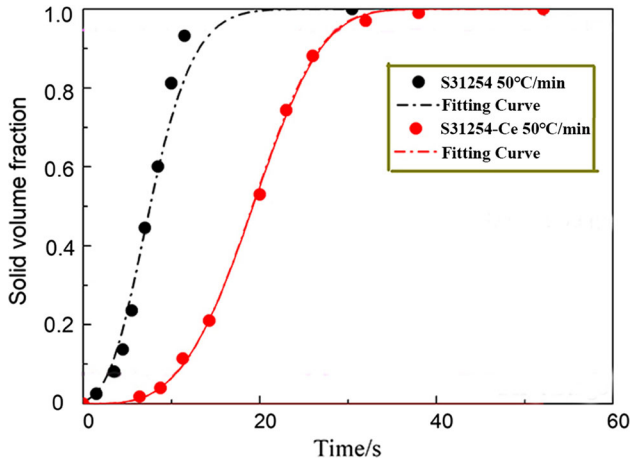


Fig. 3—Fitted curves of the solid volume fraction as a function of time.

**Table III. Fitting Results Obtained from the JMAK Model**

|           | $k$                   | $n$  | $R^2$ |
|-----------|-----------------------|------|-------|
| S31254    | $3.91 \times 10^{-3}$ | 2.6  | 0.998 |
| S31254-Ce | $1.79 \times 10^{-5}$ | 3.57 | 0.998 |

described in terms of the Johnson–Mehl–Avrami–Kolmogorov (JMAK) theory.<sup>[26]</sup> The JMAK equation is commonly expressed as Eq. [1] where  $t$  is time,  $k$  is the rate constant for solidification and  $n$  is the Avrami exponent. The Avrami exponent  $n$  could be used to analyze the mechanism of nucleation. The Avrami exponent  $n < 3$  indicates site saturation as the nucleation mechanism, which only has the initial nucleation at the start of the phase transformation. The Avrami exponent  $4 > n > 3$  indicates site saturation plus Avrami nucleation as the nucleation mechanism, which has a decreasing nucleation rate after the initial nucleation.<sup>[27]</sup> The rate constant  $k$  could represent the velocity of solid–liquid phase transformation. The rate constant  $k$  can be expressed as Eq. [2] where  $Q$  is the activation energy,  $k_0$  is the dynamic parameter,  $T$  is the thermodynamic temperature, and  $R$  is the molar gas constant. The effective overall time or temperature-dependent activation energy  $Q$  can be interpreted as a combination of the constant activation energies for nucleation and growth,  $Q_N$  and  $Q_G$ .<sup>[28,29]</sup> The fitting results are shown in Table III.

$$Y = 1 - \exp(-kt^n) \quad [1]$$

$$k = k_0 \exp\left(\frac{nQ}{RT}\right) \quad [2]$$

The Avrami exponent  $n$  is evaluated to be 2.6 and 3.57 in S31254 and S31254-Ce, respectively. This leads to a change in the mode of nucleation from site saturation to site saturation plus Avrami nucleation during the solidification after cerium addition. Thus, a small addition of cerium in steel can prolong the period of nucleation, which is beneficial for grain refinement. The rate constant  $k$  is decreased from  $3.91 \times 10^{-3}$  to  $1.79 \times 10^{-5}$ , which indicates that the phase transition from liquid to solid has a relative lower velocity after cerium addition.

To determine the activation energy  $Q$  and the dynamic parameter  $\ln k_0$ , a collection of mathematical analyses were used and are shown in Appendix A. The relationship between  $\ln\left[\frac{v}{f(Y)} * \left(\frac{dY}{dT}\right)\right]$  and  $1/T$  is expressed in Eq. [3] where  $Y$  and  $\frac{dY}{dT}$  can be calculated from Tables III and IV. The calculated results can be used for linear fitting, where  $\ln k_0$  and  $-\frac{nQ}{R}$  are the intercept and slope of the fitting result. The fitting results are shown in Figure 4 and Table IV.

$$\ln\left[\frac{v}{f(Y)} * \left(\frac{dY}{dT}\right)\right] = \ln k_0 - \left(\frac{nQ}{R}\right) \left(\frac{1}{T}\right) \quad [3]$$

As shown in Table IV, the activation energies  $Q$  for S31254 and S31254-Ce are 4.08 and 1.54 kJ/mol, respectively. The dynamic parameters  $\ln k_0$  for S31254 and S31254-Ce are 55.29 and 28.27, respectively. Cerium addition can lower the activation energy and the dynamic parameter of the solidification phase transition. From the energy barrier point of view, the solidification transition would be easier in the S31254-Ce sample. However, a relative lower rate constant  $k$  is given in S31254-Ce, which requires detailed discussion.

### C. Effect of Cerium Addition on the Nucleation Process in S31254

The nucleation process is influenced by the nucleation mode and solid–liquid interfacial energy. Inclusion-induced heterogeneous nucleation commonly occurs during solidification in cerium-containing steel. Thermodynamic calculations were carried out to evaluate the evolution of inclusions in S31254 stainless steel after

**Table IV. Fitting Results for Calculating the Values of  $Q$  and  $\ln k_0$  for S31254 and S31254-Ce**

|           | $T_s$ (°C) | $A$                    | $B$  | $R^2$ | $v$ (°C/s) | $Q$ (kJ/mol) | $\ln k_0$ |
|-----------|------------|------------------------|------|-------|------------|--------------|-----------|
| S31254    | 1354.9     | $2.49 \times 10^{-11}$ | 7.82 | 0.978 | 5/6        | 4.08         | 55.29     |
| S31254-Ce | 1371.3     | $3.69 \times 10^{-8}$  | 5.03 | 0.997 | 5/6        | 1.54         | 28.27     |

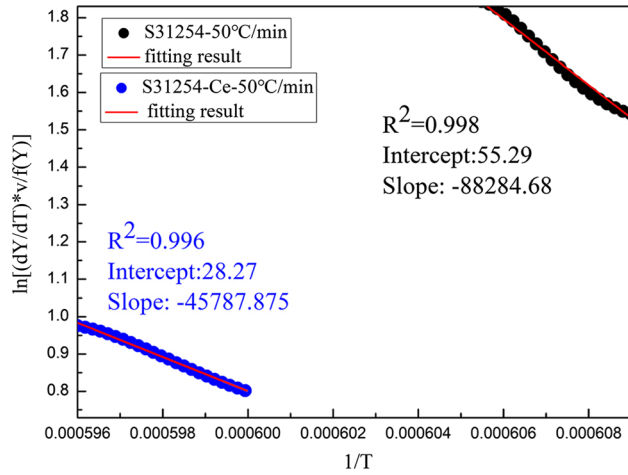


Fig. 4—Fitting results of S31254 and S31254-Ce under cooling rate of 50 °C/min.

adding a small amount of cerium. A stability diagram of Ce-Al-O was calculated by using FactSage7.0 software (Databases: FToxid, FactPS, FTmisc, Phase Diagram module) based on the chemical composition of S31254 stainless steel at 1500 °C. In Figure 5, the inclusions could transform in the order of “Slag-liq + Spinel  $\rightarrow$  MgO +  $\alpha$ -Ca<sub>2</sub>SiO<sub>4</sub> + AlCeO<sub>3</sub> + Ce<sub>2</sub>O<sub>3</sub>” after an addition of 0.013 pct Ce. Figure 6 shows the SEM-mappings of the typical inclusions in the S31254 and S31254-Ce samples. The inclusions in the S31254 sample were composed of the types of Al<sub>2</sub>O<sub>3</sub>·MgO. The shape of those inclusions is irregular, blocky and rectangular. Figure 6(b) shows the typical inclusions in the S31254-Ce sample. It was determined that shared features of the Ce<sub>2</sub>O<sub>3</sub>-Al<sub>2</sub>O<sub>3</sub>-SiO<sub>2</sub> system inclusions were a high Ce content in the inner part and right part and a high Si content in the left part. Thus, the typical type of inclusion in molten steel is changed from MgO-Al<sub>2</sub>O<sub>3</sub> to high-Ce<sub>2</sub>O<sub>3</sub> complex inclusions after cerium addition, which is consistent with the calculated results.

The inclusion disregistry can be calculated on the basis of Bramfitt’s planar lattice disregistry model<sup>[30]</sup>:

$$\delta_{(hkl)_n}^{(hkl)_s} = \sum_{i=1}^3 \frac{|(d_{[uvw]}^i_s \times \cos \theta) - d_{[uvw]}^i_n|}{3} \times 100 \quad [4]$$

$(hkl)_{s/n}$  = a low-index plane of the substrate/nucleated solid;  $[uvw]_{s/n}$  = a low-index direction in  $(hkl)_{s/n}$ ;  $d_{[uvw]}^i_{s/n}$  = the interatomic spacing along  $[uvw]_{s/n}$ ;  $\theta$  = the angle between the  $[uvw]_s$  and  $[uvw]_n$ .

An estimate of the lattice disregistry is given in Table V. AlCeO<sub>3</sub> and Ce<sub>2</sub>O<sub>3</sub> have a smaller lattice disregistry (< 12 pct) between inclusions and the austenitic phase. Nuri *et al*<sup>[8]</sup> indicate the relationship between the calculated disregistry  $\delta$  and critical undercooling temperature. As shown in Table V, the critical undercooling temperature decreases in the order of  $\alpha$ -Ca<sub>2</sub>SiO<sub>4</sub>, MgO, MgAl<sub>2</sub>O<sub>4</sub>, Ce<sub>2</sub>O<sub>3</sub> and AlCeO<sub>3</sub>. This calculated result is consistent with the initial nucleation temperature, which is obtained from *in situ* observation. Ce-containing inclusions in steel could improve the ability for austenite heterogeneous nucleation due to having part of AlCeO<sub>3</sub> or Ce<sub>2</sub>O<sub>3</sub> crystal characteristics.

Figure 7 shows the SEM-BSD photos of the samples of S31254 and S31254-Ce. The MgO-Al<sub>2</sub>O<sub>3</sub> system inclusions are mainly distributed in the boundary of grains in the sample of S31254. However, Ce-containing inclusions are mainly distributed in the interior of grains in the sample of S31254-Ce. Thus, Ce-containing inclusions could be an effective core for austenite heterogeneous nucleation. The inclusion number density and inclusion size distribution in S31254 and S31254-Ce are shown in Figure 8. Cerium addition could increase the inclusion number density from 35.7 to 81.2/mm<sup>2</sup> and decrease the inclusion size distribution, which is significant for austenite heterogeneous nucleation.

The solid-liquid interfacial energy ( $\gamma_{SL}$ ) plays an important role in the liquid solid transformation, which resists nucleation during solidification. Cerium is an interfacial active element and can modify  $\gamma_{SL}$ . However, the change in the interfacial energy during the nucleation process is difficult to obtain through an experimental method. The effect of cerium microalloying on the interfacial energy change is still unclear. Zhang *et al*<sup>[31]</sup> presented a new thermodynamic model for obtaining the solid-liquid interfacial energy based on the Warren model, which could give a way to look at the influence of cerium addition on the interfacial energy during the nucleation process. The interfacial energy contains chemical ( $\gamma_{SL(c)}$ ) and structural ( $\gamma_{SL(b)}$ ) contributions. In view of the small Gibbs energy change between the liquid and solid during the period of nucleation, the chemical contributions to the interfacial energy can be ignored.

It is assumed that the composition of the nucleus interface is the same as the steel composition except for cerium atoms. The content of cerium is enriched in the interface during nucleation due to its low solubility in austenite. Calculated parameters for the interfacial energy are shown in Table VI, and the result is shown in Figure 9. The principal components in S31254 were

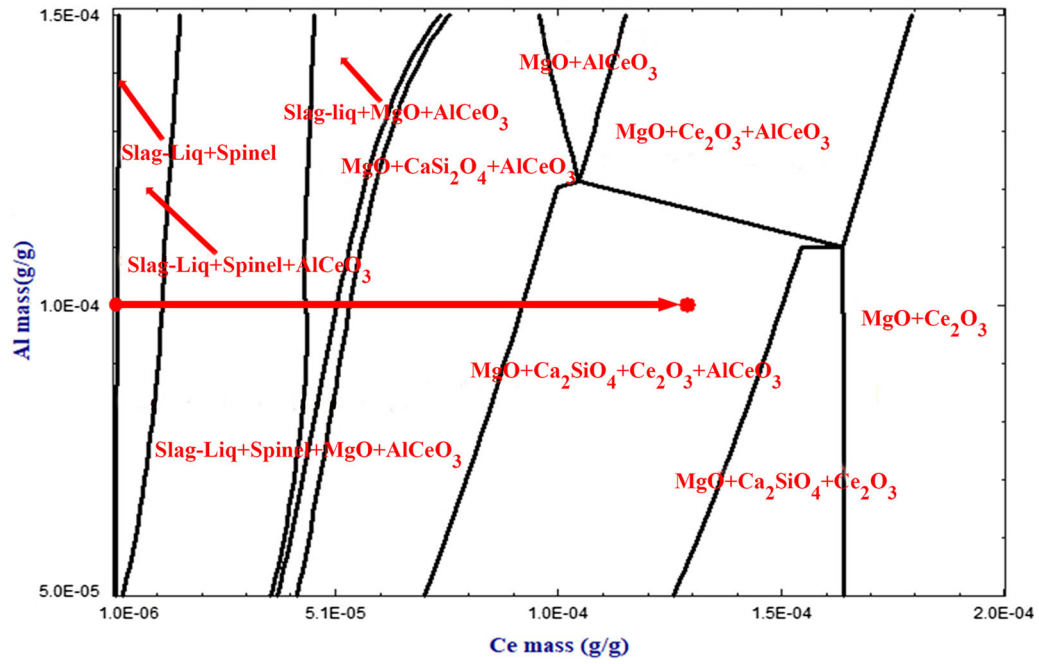


Fig. 5—Stability diagram of Ce-Al-O in S31254 stainless steel at 1500 °C.

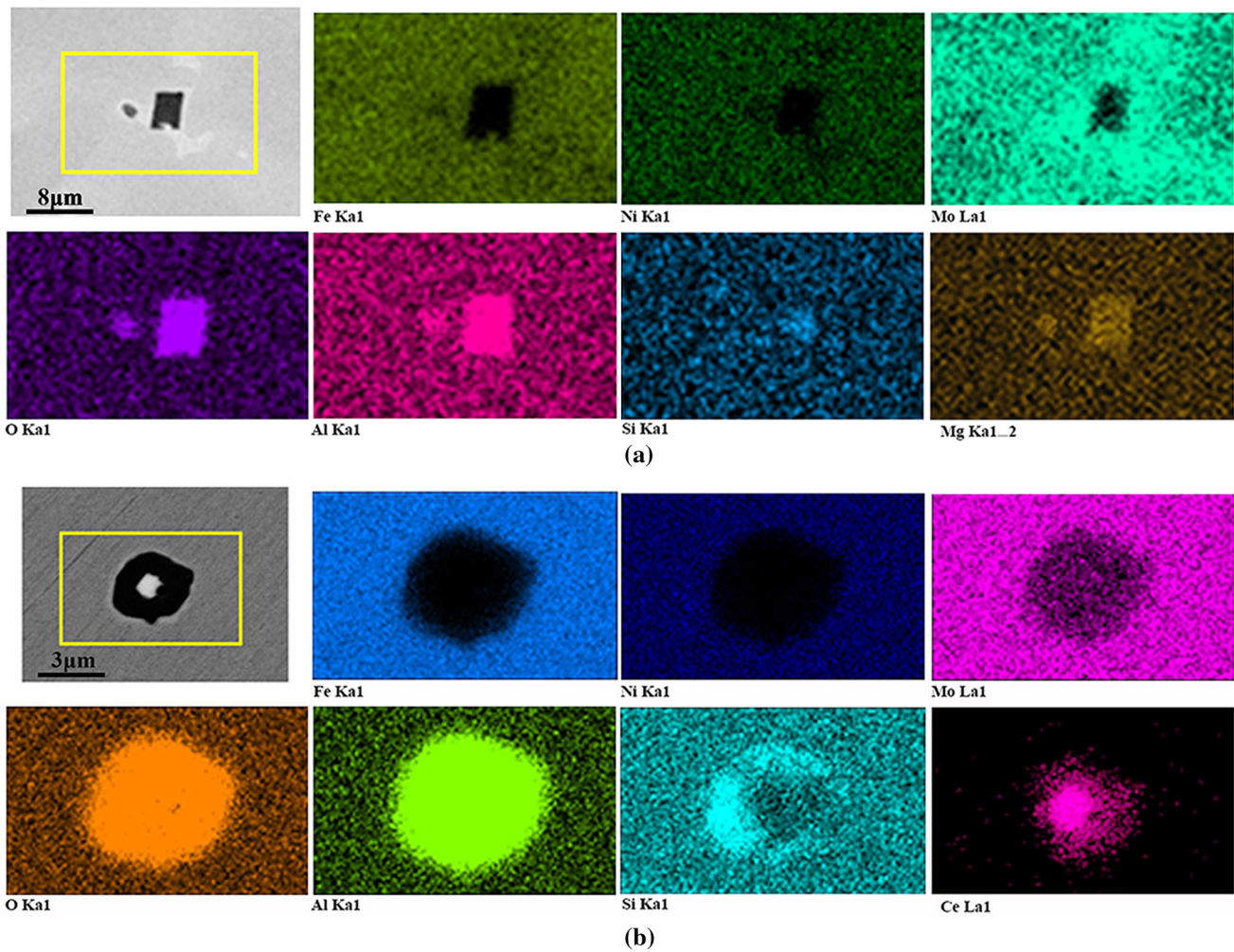
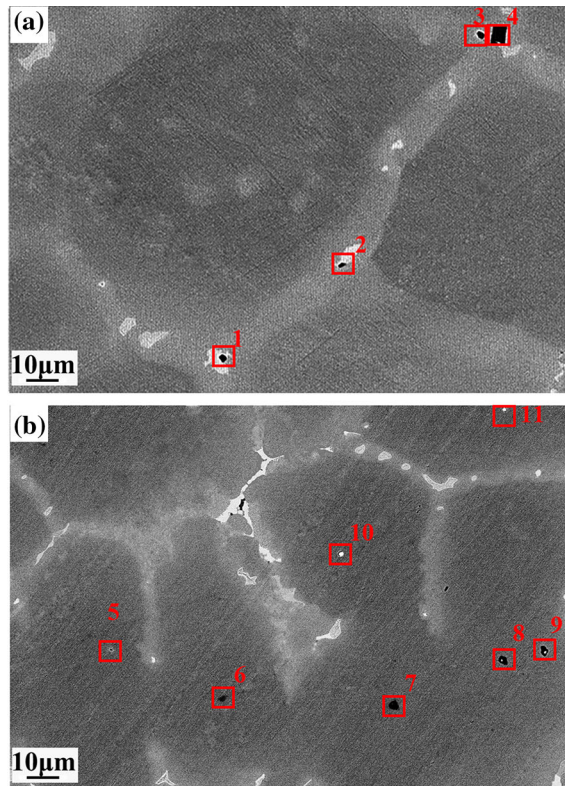


Fig. 6—SEM-mappings of typical inclusion in S31254 (a) and S31254-Ce (b).

**Table V. Lattice Disregistry Between Austenite and the Inclusions**

|  | Lattice Constant  | Orientation  | $[hkl]$ Inclusion  | $[hkl]$ Austenite   | $\theta$ (deg) | Lattice Disregistry (Pct) | $\Delta T = \frac{\delta^2}{8}$ ( $^{\circ}\text{C}$ ) |
|--|-------------------|--|--|---|----------------|---------------------------|--|
| Austenite<br>$\text{MgAl}_2\text{O}_4$ | 3.56 Å<br>8.075 Å | (011) $\text{MgAl}_2\text{O}_4$<br>//((111) $\gamma$ -Fe             | $[\bar{1}\bar{1}\bar{2}]$<br>[101]<br>[110]                              | $[\bar{1}1\bar{2}]$<br>[10 $\bar{1}$ ]<br>[1 $\bar{1}$ 0]   | 0              | 13.01                     | 21.15  |
| $\alpha$ - $\text{Ca}_2\text{SiO}_4$   | 5.532 Å           | (0001) $\alpha$ - $\text{Ca}_2\text{SiO}_4$<br>//((110) $\gamma$ -Fe | $[\bar{2}\bar{1}\bar{0}]$<br>[100]<br>[010]                              | [001]<br>[ $\bar{1}$ 11]<br>[ $\bar{1}$ 10]                 | 0<br>5<br>0    | 51.72                     | 334  |
| MgO                                    | 4.224 Å           | (100) MgO<br>//((100) $\gamma$ -Fe                                   | [001]<br>[011]<br>[010]  | [ $\bar{1}2\bar{1}$ ]<br>[ $\bar{2}$ 11]<br>[ $\bar{1}$ 01] | 0<br>15<br>0   | 16.98                     | 36.04  |
| $\text{AlCeO}_3$                       | 3.767 Å           | (100) $\text{AlCeO}_3$<br>//((100) $\gamma$ -Fe                      | [001]<br>[012]<br>[010]  | [001]<br>[011]<br>[010]                                     | 0<br>18.5<br>0 | 3.82                      | 1.82   |
| $\text{Ce}_2\text{O}_3$                | 3.941 Å           | (0001) $\text{Ce}_2\text{O}_3$<br>//((111) $\gamma$ -Fe              | $[\bar{1}\bar{2}\bar{1}\bar{0}]$<br>[ $\bar{1}$ 100]<br>[ $\bar{2}$ 100] | [ $\bar{1}$ 01]<br>[ $\bar{2}$ 11]<br>[ $\bar{1}$ 10]       | 0              | 6.8                       | 5.78   |



|           | wt | No | MgO   | $\text{Al}_2\text{O}_3$ | CaO  | $\text{SiO}_2$ | $\text{Ce}_2\text{O}_3$ |
|-----------|----|----|-------|-------------------------|------|----------------|-------------------------|
| S31254    |    | 1  | 24.8% | 75.2%                   |      |                |                         |
|           |    | 2  | 20.2% | 76.3%                   | 3.5% |                |                         |
|           |    | 3  | 22.9% | 77.1%                   |      |                |                         |
|           |    | 4  | 23.7% | 71.2%                   | 2.4% | 2.7%           |                         |
| S31254-Ce |    | 5  | 0.6%  | 19.5%                   | 0.4% | 17.4%          | 62.1%                   |
|           |    | 6  | 1.1%  | 30.2%                   | 2.1% | 7.2%           | 59.4%                   |
|           |    | 7  | 0.8%  | 34.9%                   | 3.6% | 5.1%           | 55.6%                   |
|           |    | 8  | 1.2%  | 27.3%                   | 5.1% | 3.3%           | 62.1%                   |
|           |    | 9  | 4.7%  | 34.1%                   | 2.8% | 2.2%           | 56.2%                   |
|           |    | 10 | 1.4%  | 41.9%                   |      |                | 56.6%                   |
|           |    | 11 |       | 12.8%                   |      |                | 87.2%                   |

Fig. 7—SEM-BSD photos in the sample of (a) S31254, (b) S31254-Ce, and (c) inclusion composition.

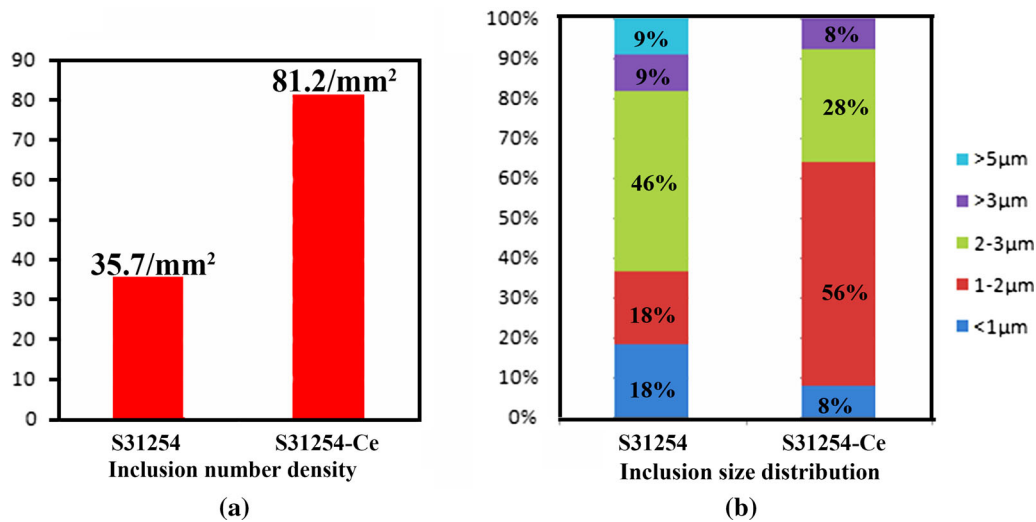


Fig. 8—(a) Inclusion number density and (b) size distribution in S31254 and S31254-Ce.

Table VI. Calculated Parameters for Interfacial Energy

|  | Fe    | Cr    | Ni    | Mo    | Ce    |
|--|-------|-------|-------|-------|-------|
| $\gamma_{SL(B)}^i$ (J/m <sup>2</sup> ) | 0.278 | 0.331 | 0.279 | 0.380 | 0.087 |

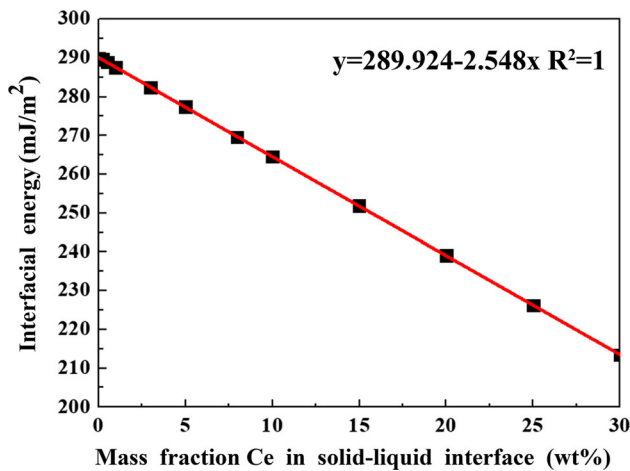


Fig. 9—The interfacial energy with respect to cerium enrichment in the solid-liquid interface.

used to calculate the interfacial energy. As shown in Table VI, cerium has a relatively lower structure interfacial energy than any other main components.

As shown in Figure 9, the interfacial energy is reduced from 289.92 to 287.37 mJ/m<sup>2</sup> when the cerium content is increased from 0 to 1 wt pct in the solid-liquid interface.

The interfacial activity  $J$  ( $J = \frac{d_{\gamma/SL}}{d_{[x]}}$ ) is an important index for measuring the influence of any elemental addition in an alloy on the solid-liquid interfacial energy.  $J_u$  is the slope of the relationship between  $w_{Ce}$

and  $\gamma_{SL}$ , which can be obtained from linear fitting. As shown in Figure 7,  $J = -2.548$  mJ/m<sup>2</sup>. The interfacial energy ( $\gamma_{SL}$ ) decreases with the enrichment of cerium in the interface, which is beneficial for austenitic nucleation; however, the variation in the interfacial energy is small due to the nucleation process.

In summary, Ce-containing inclusions in S31254-Ce improve the ability for austenite heterogeneous nucleation, which would significantly reduce the energy barrier of nucleation. Moreover, the solid-liquid interfacial energy is reduced with the increase of the cerium content in the solid-liquid interface, but the change is small due to the nucleation process.

#### D. Effect of Cerium Addition on Austenite Grain Growth in S31254

Typical growth processes of a single grain in S31254 and S31254-Ce are shown in Figure 10. As shown in Figure 10(a), the primary austenite starts to nucleate and then exhibits continual growth in all directions. At the same cooling rate, grain growth exhibits a different mode in the S31254-Ce sample. The primary austenite is observed in the shape of a crescent, and then, it bends to form the shape of a circle. After forming the circle-shaped primary austenite, the primary phase consumes all of the liquid phase in the circle and grows outward until it touches the other primary phases.

The growth velocity of a single grain is measured from Figure 10 and shown in Figure 11. As shown in Figure 11(a), the growth velocity of a single grain in S31254 is approximately 20  $\mu$ m/s. The growth velocity at the tip and interface is obviously reduced to approximately 2  $\mu$ m/s for the sample of S31254-Ce. As shown in Figure 11(b), the primary austenite has a much larger growth velocity at the tip than in the middle, which makes it form into the shape of a circle. Thus, cerium addition limits the growth of austenite grains and causes the solidified structure to become thinner.



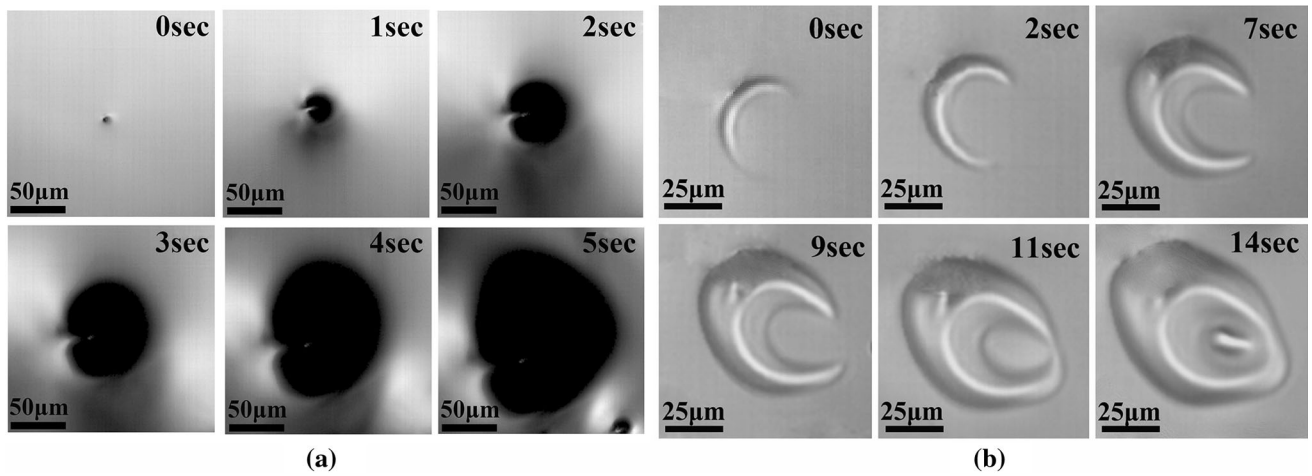


Fig. 10—HT-LSCM observation of the growth process of a single austenite grain cooled at 50 °C/min in (a) S31254 and (b) S31254-Ce stainless steel.

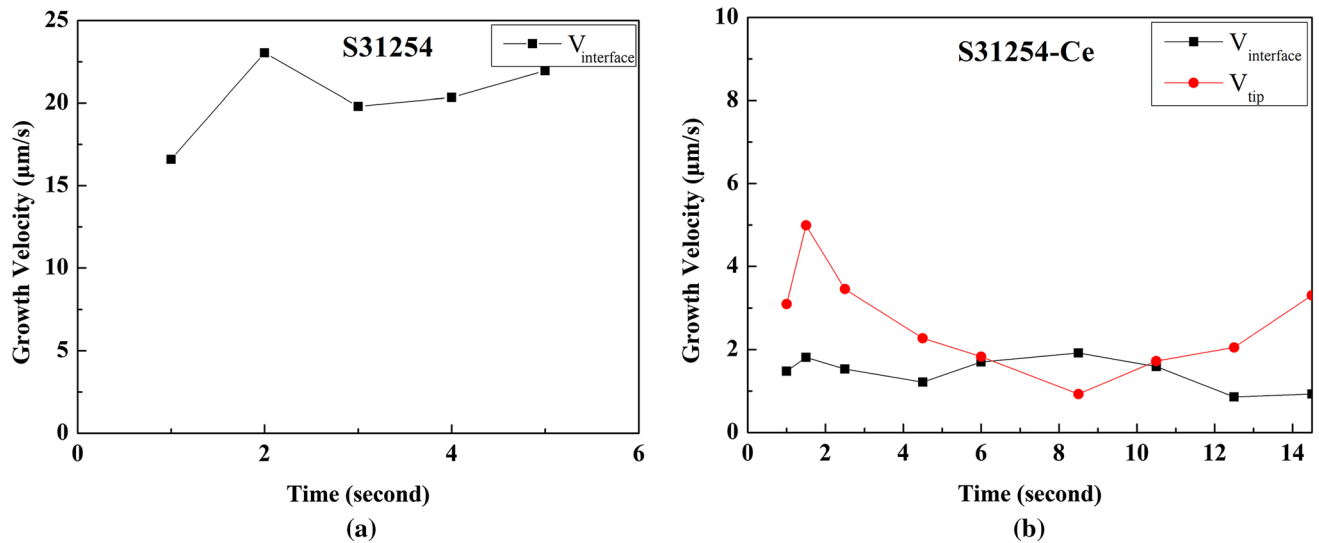


Fig. 11—Growth velocity of a single grain in (a) S31254 and (b) S31254-Ce.

Table VII. Calculated Parameters for  $\Delta T_{\max}^c$

|                     | Cr    | Ni     | Mo    | Ce     |
|---------------------|-------|--------|-------|--------|
| $c_0$               | 20    | 18     | 6     | 0.013  |
| $m_i$               | - 1.3 | - 3.9  | - 2.8 | - 11.5 |
| $k_i$               | 0.89  | 1.02   | 0.68  | 0.01   |
| $\Delta T_{\max}^c$ | 3.21  | - 1.37 | 7.90  | 14.95  |

A possible reason for the inhibition of grain growth during the solidification process is bigger constitutional undercooling ( $\Delta T_{\max}^c$ ) at the solid-liquid interface caused by cerium addition. The addition of solute elements generates constitutional undercooling in a diffusion layer ahead of the advancing solid/liquid

interface, which restricts grain growth since the diffusion of the solute occurs slowly, thus limiting the rate of crystal growth. In addition, further nucleation occurs in front of the interface because nucleants in the melt are more likely to survive and be activated.<sup>[32]</sup> It has been shown in Figure 2(d) that new nucleants could be observed in front of the other primary phase. The max constitutional undercooling can be calculated through Eq. [5]. The thermodynamic data listed in Table VII were calculated by using Thermo-Calc software

$$\Delta T_{\max}^c = \frac{\sum C_0^i \times m_i \times (k_i - 1)}{k_i} \quad [5]$$

where  $C_0^i$  is the initial composition of element  $i$ ,  $m_i$  is the liquidus slope of element  $i$ , and  $k_i$  is the equilibrium partition coefficient of element  $i$ .

As shown in Table VII, the value of  $\Delta T_{\max}^c$  in S31254 is mainly influenced by Mo ( $\Delta T_{\max}^c = 7.9$ ) due to the relatively low  $k_{\text{Mo}} = 0.68$ . However, a higher value of  $\Delta T_{\max}^c = 14.95$  is obtained after 0.013 pct cerium addition due to that the value of  $k_{\text{Ce}}$  is much less than 1 in austenite. Thus, cerium addition could significantly increase the value of  $\Delta T_{\max}^c$  from 9.74 to 24.69, which indicates that S31254-Ce steel could have a much higher  $\Delta T_{\max}^c$  than that of S31254, and would further reduce the growth velocity for austenite grain growth. Furthermore, the low growth velocity for austenite grains and significantly high nucleation site density would exhibit a low rate constant  $k$  during the solidification process.

The cerium element would be enriched in the solid-liquid interface, which reduces the growth velocity for austenite grain growth. The density of cerium atoms is much lower inside the liquid zone than at the interface, and the tip shape has the lowest resistance, which makes the primary austenite form into the shape of a crescent. Thus, the primary austenite has a much larger growth velocity at the tip than in the middle, which makes it form the shape of a circle.

#### IV. CONCLUSION

The effects of cerium on the solidification behavior of S31254 stainless steel were investigated by *in situ* investigations and theoretical calculations. The main results are summarized as follows:

1. Cerium addition is highly beneficial for the nucleation sites. The initial nucleation temperature was increased by 32.3 °C, and the nucleation site density increased by 162.68/mm<sup>2</sup> after 2 seconds in the S31254-Ce sample. The Avrami exponent  $n$  changes from 2.6 to 3.57 after cerium addition, which indicates that the nucleation mechanism changes from site saturation to site saturation plus Avrami nucleation. The activation energy  $Q$  of the solidification phase transition is decreased from 4.08 to 1.54 kJ/mol after cerium addition to the molten stainless steel. Cerium in the steel melt can change the types of inclusions from MgO-Al<sub>2</sub>O<sub>3</sub>-type inclusions to Ce-containing inclusions. Those inclusions in S31254-Ce improve the ability for austenite heterogeneous nucleation, which would significantly reduce the energy barrier of nucleation. Moreover, the solid-liquid interfacial energy is reduced with the increase of the cerium content in the solid-liquid interface, but the change is small due to the nucleation process.
2. Cerium addition could significantly inhibit primary austenite grain growth. Cerium addition could prolong the entire solidification temperature range from 28 °C to 43.9 °C and limit the growth velocity of austenite grains from approximately 20 to 2 μm/s. The ratio of solid phase is reduced from 60 to 8.2 pct, but the grain density is enhanced from 68.8 to 280/mm<sup>2</sup>, with the solidification time extended to 8 sec-

onds after cerium addition. Thus, the main solidification behavior in the early solidification stage of S31254-Ce is nucleation instead of primary grain growth. The low growth velocity for austenite grains and significantly high nucleation site density would exhibit a low rate constant  $k$  during the solidification process, which indicates that the phase transition from liquid to solid has a relative lower velocity. The value of  $k$  is decreased from  $3.91 \times 10^{-3}$  to  $1.79 \times 10^{-5}$  after cerium addition.

#### ACKNOWLEDGMENTS

The authors would like to express their appreciation to the National Nature Science Foundation of China (Grant Nos. U1810207, 51774027, and 51734002), Fundamental Research Funds for the Central Universities (Grant No. FRF-TP-18-012B1), and the National Key Research and Development Program of China (Grant No. 2016YFB0300204).

#### APPENDIX A

The equation is commonly expressed as Eq. [A1], where  $t$  is the time,  $k$  is rate constant and  $n$  is the Avrami exponent. The rate constant  $k$  can be expressed as Eq. [A2], where  $Q$  is the activation energy,  $k_0$  is the dynamic parameter,  $T$  is the thermodynamic temperature, and  $R$  is the molar gas constant. The fitting results are shown in Table II.

$$Y = 1 - \exp(-kt^n) \quad [\text{A1}]$$

$$k = k_0 \exp\left(-\frac{Q}{RT}\right) \quad [\text{A2}]$$

An equation was utilized to obtain the expressions of temperature ( $T$ ) and solid phase ratio ( $Y$ ). The fitting results are available in Figure A1(b).

$$Y = \exp(-A \times (T - T_s)^B) \quad [\text{A3}]$$

where  $A$  and  $B$  are constants,  $T_s$  is the solidus temperature.

Then, the derivative of both sides of Eq. [A1] is taken, as shown in Eq. [A4].  $f(Y)$  is an implicit function of  $Y$ , and it can be expressed as shown in Eq. [A5].

$$\frac{dY}{dt} = kf(Y) \quad [\text{A4}]$$

$$f(Y) = n(1 - Y)[- \ln(1 - Y)]^{\frac{n-1}{n}} \quad [\text{A5}]$$

Moreover, the following expression can be obtained:

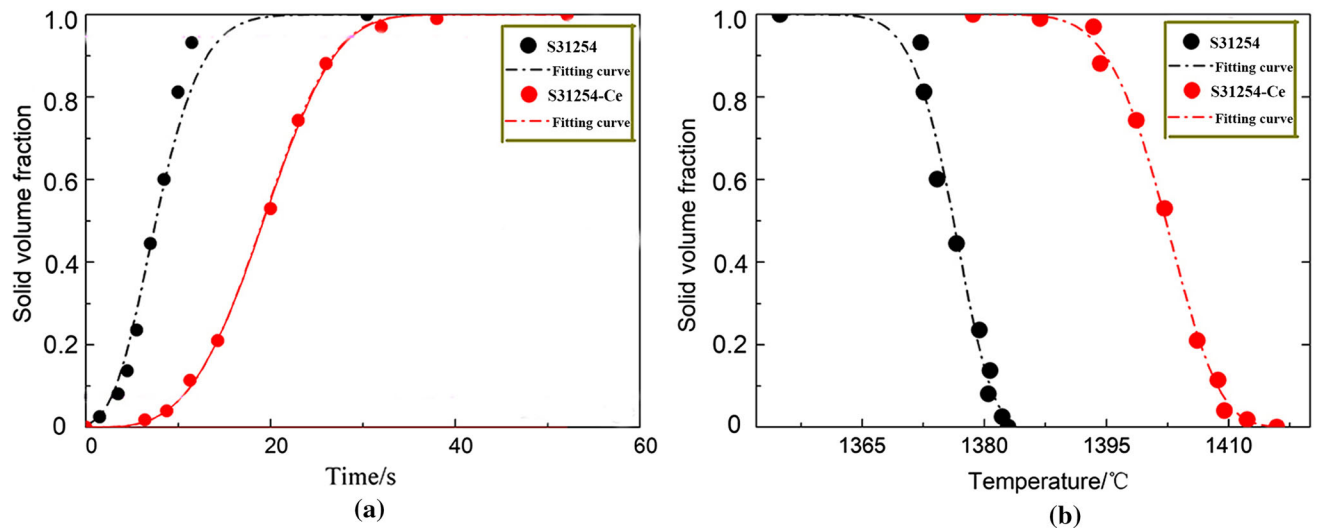


Fig. A1—Fitted curves of the solid volume fraction as a function of (a) time and (b) temperature.

$$\frac{dY}{dt} = \left(\frac{dY}{dT}\right) * \left(\frac{dT}{dt}\right) = v * \left(\frac{dY}{dT}\right) \quad [\text{A6}]$$

According to Eqs.[A4], [A5] and [A6], the relationship between  $\ln\left[\frac{v}{f(Y)} * \left(\frac{dY}{dT}\right)\right]$  and  $1/T$  is expressed in Eq. [A7], where  $Y$  and  $\frac{dY}{dT}$  are expressed in Eqs. [A2] and [A8], respectively. The linear part can be used for linear fitting, where  $\ln k_0$  and  $-\frac{Q}{R}$  are the intercept and slope of the fitting result, and the results are shown in Figure.5 and Table III.

$$\ln\left[\frac{v}{f(Y)} * \left(\frac{dY}{dT}\right)\right] = \ln k_0 - \left(\frac{Q}{R}\right) \left(\frac{1}{T}\right) \quad [\text{A7}]$$

$$\frac{dY}{dT} = \exp\left(-A(T - T_s)^B \times (-AB) \times (T - T_s)\right)^{B-1} \quad [\text{A8}]$$

## REFERENCES

1. T. Koutsoukis, A. Redjambia, and G. Fourlaris: *Mater. Sci. Eng., A*, 2013, vol. 561, pp. 477–85.
2. E.X. Pu, W.J. Zheng, Z.G. Song, J.Z. Xiang, and X.P. Wei: *J. Iron. Steel Res. Int.*, 2014, vol. 21, pp. 975–82.
3. H.B. Li, B. Zhang, Z. Jiang, S. Zhang, and Q. Lin: *J. Alloy. Compd.*, 2016, vol. 686, pp. 326–38.
4. H.C. Zhu, H.B. Li, S.C. Zhang, K.B. Li, G.H. Liu, and Z.H. Jiang: *Ironmaking Steelmaking*, 2015, vol. 10, pp. 748–55.
5. F. Tehovnik, J. Burja, B. Arh, and F. Vode: *Metallurgija.*, 2017, vol. 56, pp. 63–66.
6. R.W. Fonda, E.M. Lauridsen, W. Ludwig, P. Tafforeau, and G. Spanos: *Metall. Mater. Trans. A*, 2007, vol. 38A, pp. 2721–26.
7. H.B. Li, S. Yang, S. Zhang, B. Zhang, Z. Jiang, H. Feng, P.D. Han, and J.Z. Li: *Mater. Des.*, 2017, vol. 118, pp. 207–17.
8. Y.P. Ji, M.X. Zhang, and H.P. Ren: *Metals.*, 2018, vol. 8, pp. 884–96.
9. J.S. Park, C. Lee, and J.H. Park: *Metall. Mater. Trans. B*, 2012, vol. 43B, pp. 1550–64.
10. K. Nakajima, H. Ohta, H. Suito, and P. Jönsson: *ISIJ Int.*, 2006, vol. 46, pp. 807–13.
11. K. Sakata and H. Suito: *Metall. Mater. Trans. B*, 1999, vol. 30B, pp. 1053–63.
12. J.H. Park: *CALPHAD*, 2011, vol. 35, pp. 455–62.
13. Y. Hou and G. Cheng: *Metall. Mater. Trans. B*, 2019, vol. 50B, pp. 1351–64.
14. J.L. Caron, S.S. Babu, and J.C. Lippold: *Metall. Mater. Trans. A*, 2011, vol. 42, pp. 4015–31.
15. H.K. Sung, S.Y. Shin, W. Cha, K. Oh, S. Lee, and N.J. Kim: *Mater. Sci. Eng., A*, 2011, vol. 528, pp. 3350–57.
16. H. Terasaki and Y. Komizo: *Sci. Technol. Weld. Join.*, 2006, vol. 11, pp. 561–66.
17. T. Yamada, H. Terasaki, and Y. Komizo: *Sci. Technol. Weld. Join.*, 2008, vol. 13, pp. 118–25.
18. H. Suito, A.V. Karasev, M. Hamada, R. Inoue, and K. Nakajima: *ISIJ Int.*, 2011, vol. 51, pp. 1151–62.
19. Q. Wang, X. Zou, H. Matsuura, and C. Wang: *Metall. Mater. Trans. B*, 2018, vol. 49B, pp. 18–22.
20. T. Koseki and G. Thewlis: *Mater. Sci. Technol.*, 2005, vol. 21, pp. 867–79.
21. M.X. Guo and H. Suito: *ISIJ Int.*, 1999, vol. 39, pp. 722–29.
22. Y. Cai, Z. Luo, Z. Huang, and Y. Zeng: *J. Mater. Process. Technol.*, 2016, vol. 230, pp. 80–87.
23. C.V.D. Eijk, J. Walmsley, Electric Furance Conference. 2001, vol 59.
24. X. Shi, S.C. Duan, W.S. Yang, H.J. Guo, and J. Guo: *Metall. Mater. Trans. B*, 2018, vol. 49B, pp. 1883–97.
25. L.J. Wang, Q. Wang, J.M. Li, and K.C. Chou: *J. Mining Metall Sect. B*, 2011, vol. 52, pp. 35–40.
26. J.W. Christian: *The Theory of Transformations in Metals and Alloys, 2nd Edition, Part I*, 2nd ed., Pergamon, Oxford, 1975.
27. F. Liu, F. Sommer, and E.J. Mittemeijer: *J. Mater. Sci.*, 2007, vol. 42, pp. 573–87.
28. A.T.W. Kempen, F. Sommer, and E.J. Mittemeijer: *J. Mater. Sci.*, 2002, vol. 37, pp. 1321–32.
29. F. Liu, F. Sommer, and E.J. Mittemeijer: *J. Mater. Sci.*, 2004, vol. 39, pp. 1621–34.
30. B.L. Bramfitt: *Metall. Trans.*, 1970, vol. 1, pp. 2958–58.
31. C. Zhang and Y. Du: *Metall. Mater. Trans. A*, 2017, vol. 48A, pp. 5766–70.
32. Y.C. Lee, A.K. Dahle, and D.H. Stjohn: *Metall. Mater. Trans. A*, 2000, vol. 31A, pp. 2895–2906.

**Publisher's Note** Springer Nature remains neutral with regard to jurisdictional claims in published maps and institutional affiliations.